# Set-based corral control in stochastic dynamical systems: Making almost invariant sets more invariant

Eric Forgoston,[1,a)] Lora Billings,[1] Philip Yecko,[1] and Ira B. Schwartz[2]
[1]*Department of Mathematical Sciences, Montclair State University, 1 Normal Avenue, Montclair, New Jersey 07043, USA*
[2]*Nonlinear Systems Dynamics Section, Plasma Physics Division, Code 6792, U.S. Naval Research Laboratory, Washington, DC 20375, USA*

We consider the problem of stochastic prediction and control in a time-dependent stochastic environment, such as the ocean, where escape from an almost invariant region occurs due to random fluctuations. We determine high-probability control-actuation sets by computing regions of uncertainty, almost invariant sets, and Lagrangian coherent structures. The combination of geometric and probabilistic methods allows us to design regions of control, which provide an increase in loitering time while minimizing the amount of control actuation. We show how the loitering time in almost invariant sets scales exponentially with respect to the control actuation, causing an exponential increase in loitering times with only small changes in actuation force. The result is that the control actuation makes almost invariant sets more invariant. © *2011 American Institute of Physics*. [doi:10.1063/1.3539836]

**Prediction and control of the motion of an object in time-dependent and stochastic environments is an important and fundamental problem in nonlinear dynamical systems. One of the main goals of control is the design of a theory that can take unstable states and render them stable. For example, small perturbations at the base of an inverted pendulum will stabilize the inverted state. Noise poses a greater problem for deterministically controlled states, in that stochastic effects destabilize the states as well as their neighborhoods. Therefore, control theory of stochastic dynamical systems may be addressed by examining the change in stability of certain sets. We present a variety of geometric and probabilistic set-based methods that enable one to compute controllable sets. For a particle moving under the influence of deterministic and stochastic forces with no control, these sets determine regions which are unstable in the sense that the particle will leave the set after a sufficiently long time. Controls added to particle dynamics, to increase the time to escape (or loitering time), have a strong dependence on the probabilistic and geometric set characteristics. The determination of controls and associated sets allow for an increase in the amount of time the particle can loiter in a particular region while minimizing the amount of control actuation. Our theoretical analysis shows how an increase in the strength of the control force leads to a decrease in the probability that an object will escape from the control region. In fact, we have found that small changes in the control actuation force have an exponential effect on the loitering time of the object. Additionally, we show how the exponential increase in escape times from the controlled sets is related to the problem of noise-induced escape from a potential well.**

## I. INTRODUCTION

Ocean circulation impacts weather, climate, marine fish and mammal populations, and contaminant transport, making ocean dynamics of great industrial, military, and scientific interest. A major problem in the field of ocean dynamics involves forecasting, or predicting, a variety of physical quantities, including temperature, salinity, and density. By fusing recently measured data with detailed flow models, it is possible to achieve improved prediction. Therefore, forecasts occur with increased accuracy.[1] As a result, ocean surveillance may be improved by incorporating the continuous monitoring of a region of interest.

Researchers have used surface drifters and submerged floats to acquire data for many years. More recently, sensing platforms such as autonomous underwater gliders[2–4] have been developed. The gliders can operate in both littoral (coastal) and deep-ocean regimes, and may be used for data acquisition, surveillance, and reconnaissance. One drawback in the use of gliders involves their limited amount of total control actuation due to energy constraints, such as short battery life. For applications such as regional surveillance, energy constraints may be alleviated by taking advantage of the dynamical flow field structures and their respective body forces.

Autonomous underwater gliders are subjected to drift due to hydrodynamic forces. This drift can be extremely complicated since the velocity fields found in the ocean are aperiodic in time and feature a complex spatial structure. Instead of constantly reacting to the drift (and thereby expending energy), one can minimize the glider's energy expenditure by taking advantage of the underlying structure found in geophysical flows. However, in order to harness the ocean forces to minimize energy expenditure during control actuation, one needs to analyze the structures from the correct dynamical viewpoint.

a)Electronic mail: eric.forgoston@montclair.edu.

The potential for dynamical systems tools to shed light on complex, even turbulent, flow fields such as ocean dynamics, has been understood for decades. Work in this area has intensified in the past decade with a new focus placed on the improved Lagrangian perspective that dynamical systems approaches may provide, especially for complex, aperiodic flows in which the traditional Eulerian perspective on the flow is unhelpful or even misleading. During boundary layer separation, for example, sheet-like flow structures coincide with fluid particles being ejected from the wall region, a technologically important feature that an Eulerian framework fails to capture in unsteady cases, but which has a clear Lagrangian signature that can be identified using finite-time Lyapunov exponents (FTLE).[5] In liquid jet breakup, a similar ejection process occurs during primary atomization, but a limited Lagrangian perspective is provided by the liquid–gas interface, revealing liquid sheets and ligaments that precede droplet formation.[6] The development of these critical fluid sheets and ligaments can be traced to unsteady, finite-amplitude global flow structures.[7] Dynamical systems tools thus provide a new approach to the characterization and control of these important flows. Geophysical flows offer another example where an Eulerian framework is ineffective in the diagnosis of large Lagrangian structures and the measurement of transport. For prediction and control of particle dynamics in large surveillance regions of interest, Lagrangian structures of geophysical flows need to be characterized in both deterministic and stochastic settings.

The field of geophysical fluid dynamics (GFD) involves the study of large-scale fluid flows that occur naturally. GFD flows are, by nature, aperiodic and stochastic. The data sets describing them are usually finite-time and of low resolution. Established tools of dynamical systems have proven to be less effective in these cases: while providing some insight, they cannot provide realistic or detailed flow field data relevant to the trajectories of tracer particles. For this, dynamical systems tools can be applied to fluid flows in an alternative way, by interpreting the Eulerian flow field $\mathbf{u}(\mathbf{x}, t)$ as a dynamical system $\mathbf{x}' = \mathbf{u}(\mathbf{x}, t)$ describing the trajectories of tracer particles. The phase space and real space are identical here and due to the incompressibility condition $\nabla \cdot \mathbf{u} = 0$, the resulting dynamical system is conservative. This "chaotic advection" approach originated with Aref[8] and demonstrated that even simple laminar two-dimensional (2D) periodic and three-dimensional (3D) steady flows[9] could lead to complex, chaotic particle trajectories. Figure 1 illustrates an example of how particles in a periodic flow may exhibit unexpected trajectories. In this figure, a single-layer quasi-geostrophic beta plane is being driven by a bimodal wind-stress with a small amplitude periodic perturbation. Details of this ocean model can be found in the Appendix.

In the last two decades, this approach has led to new tools including the study of transport by coherent structures,[10] lobe dynamics,[11] distinguished trajectories,[12] and global bifurcations.[13,14] Even though the transport controlling structures in GFD flows are inherently complicated and unsteady, their understanding is necessary to the design of glider controls. To overcome this obstacle we combine a set of dynamical systems tools that have proven effective in higher dimensions[15] and stochastic problems.[16,17]
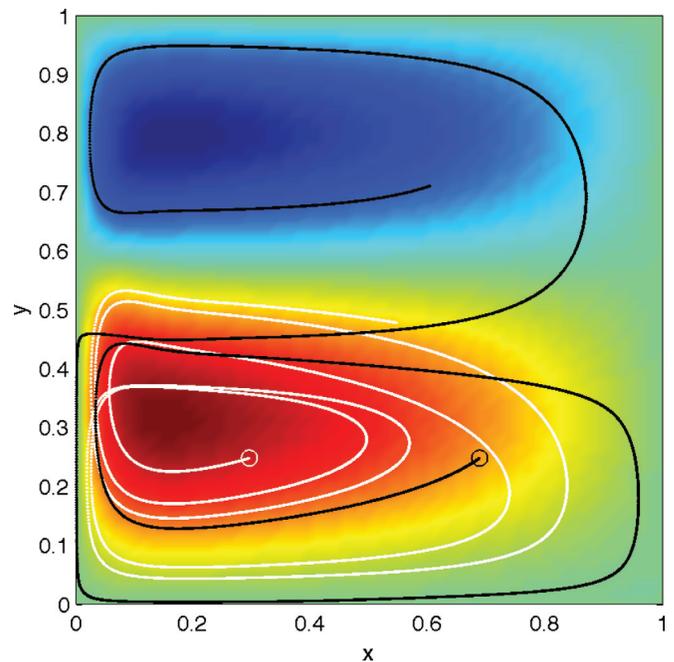


FIG. 1. (Color online) Streamfunction (background color) and two particle trajectories within a single-layer quasi-geostrophic ocean model (see Appendix) subject to low-amplitude periodic forcing whose mean gives a steady double-gyre/western boundary current flow solution. Initial points on the trajectory are identified with open circles.

In this paper, we will consider a well-known driven double-gyre flow as an example to illustrate our prediction/control framework.[18] This model can be thought of as a simplified version of the double-gyre shown in Fig. 1 which is a solution to a realistic quasi-geostrophic ocean model. It should be noted that our methods are general and may be applied to any flow of interest. The goal of our approach is the production of a complete picture of particle trajectories and tracer lingering times, which enables one to design a control strategy that limits tracers from switching between gyres.

The techniques we will use to analyze the dynamical systems are based on both deterministic and stochastic analysis methods, and reveal different structures depending on the system under examination. In the deterministic case, the Lagrangian coherent structures (LCS) reveal much about transport and information related to the basin boundaries. They also pinpoint regions of local sensitivity in the phase space of interest. Since basin boundaries are most sensitive to initial conditions, uncertainties in the data near the boundaries generate obstructions to predictability. Therefore, highly uncertain regions in phase space may be revealed by computing local probability densities of uncertain regions in the deterministic case, but using noisy initial data. Finally, in the time-dependent stochastic case, we can describe which sets contain very long term, albeit finite, trajectories. The sets are almost invariant due to the stochastic forcing on the system, which causes random switching between the almost invariant sets. The tools we use here are based on the stochastic Frobenius–Perron (SFP) operator theory. Once the full structure of almost invariant sets is identified along with regions of high uncertainty, control strategies may be designed to maintain long time trajectories within a given region with minimal actuation. In

Fig. 1, one can see that one particle's trajectory remains in the lower gyre for a long period of time, while the other particle escapes from the lower gyre to the upper gyre. The tools we will develop and outline in this article will enable one to know if and when a control force must be actuated to prevent the particle from escaping.

The layout of the paper is as follows. In Sec. II we present the stochastic double-gyre system and examine the deterministic dynamical features. In Sec. III, we show how to use the FTLE to describe transport, and we show in Sec. IV how to quantify uncertainty regions. We then turn to the stochastic system, and describe in Sec. V how to compute almost invariant sets. Section VI contains a discussion of our corral control strategy and Sec. VII contains the conclusions and discussion.

## II. THE MODEL

A simple model of the wind-driven double-gyre flow is provided by

$$\dot{x} = -\pi A \sin(\pi f(x,t))\cos(\pi y) - \alpha x + \eta_1(t), \quad (1a)$$

$$\dot{y} = \pi A \cos(\pi f(x,t))\sin(\pi y)\frac{df}{dx} - \alpha y + \eta_2(t), \quad (1b)$$

$$f(x,t) = \epsilon \sin(\omega t + \psi)x^2 + (1 - 2\epsilon \sin(\omega t + \psi))x. \quad (1c)$$

When $\epsilon = 0$, the double-gyre flow is time-independent, while for $\epsilon \neq 0$, the gyres undergo a periodic expansion and contraction in the $x$ direction. In Eqs. (1a)–(1c), $A$ approximately determines the amplitude of the velocity vectors, $\omega/2\pi$ gives the oscillation frequency, $\epsilon$ determines the amplitude of the left-right motion of the separatrix between the two gyres, $\psi$ is the phase, $\alpha$ determines the dissipation, and $\eta_i(t)$ describes a stochastic white noise with mean zero and standard deviation $\sigma = \sqrt{2D}$, for noise intensity $D$. This noise is characterized by the following first and second order statistics: $\langle \eta_i(t) \rangle = 0$ and $\langle \eta_i(t)\eta_j(t') \rangle = 2D\delta_{ij}\delta(t-t')$ for $i = 1, 2$. In the rest of the article we shall use the following parameter values: $\alpha = 0.005$, $A = 0.1$, $\epsilon = 0.15$, and $\omega = 2\pi/20$. We consider the dynamics restricted to the domain $\{(x, y)|0 \leq x \leq 2 \text{ and } 0 \leq y \leq 1\}$. An unforced, undamped autonomous version of the double-gyre model was studied by Rom-Kedar et al.[19] and an undamped system with different forcing was studied by Froyland and Padberg.[20]

Prior to defining the control of certain sets of the stochastic system, we first describe the important dynamical features of the deterministic part of Eqs. (1a)–(1c). There are two attracting periodic orbits, which correspond to two fixed points of the Poincaré map defined by sampling the system at the forcing period. For each fixed point, there corresponds a left and a right basin of attraction. Local analysis on the Poincaré section about the fixed points reveals the attractors to be spiral sinks, which generate the global double-gyre. A representative basin map at the phase $\psi = 0$ is shown in Fig. 2. One can see the complicated basin boundary structure in which the basins of attraction are intermingled, a signature of the existence of a fractal basin boundary. There are also several unstable (saddle) periodic orbits corresponding to fixed points that lie along or close to the domain boundary.
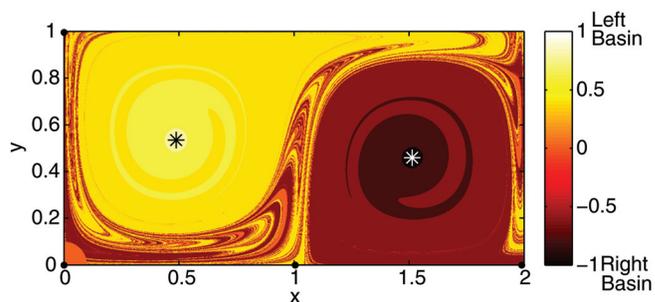


FIG. 2. (Color online) The basin Poincaré map for the deterministic part of Eqs. (1a)–(1c) at phase $\psi = 0$. The locations of the attracting fixed points corresponding to periodic orbits are denoted by the stars. The color represents the convergence rate to the attractors. As shown by the color bar, positive values converge to the left basin and negative values converge to the right basin. The largest magnitude values converge the fastest. Four saddle fixed points are located within the boundaries of the domain, and are denoted by large dots. The remaining two are located at (0.995, 1.005) and (2.010, 0.995).

Due to the intermingling of the basin boundaries, one can expect that small perturbations, or uncertainties, in initial conditions near the basin boundary will generate large changes in dynamical behavior. This can occur deterministically, or when noise is added to the system. Therefore, we quantify regions of uncertainty in phase space in both deterministic and stochastic settings in Secs. IV and V, respectively.

## III. FINITE-TIME LYAPUNOV EXPONENTS

One method that can be used to understand transport and which quantifies localized sensitive dependence to initial conditions in a given fluid flow involves the computation of FTLE. In a deterministic setting, the FTLE also gives an explicit measure of phase space uncertainty. Given a dynamical system, one is often interested in determining how particles that are initially infinitesimally close behave as time $t \to \pm \infty$. It is well-known that a quantitative measure of this asymptotic behavior is provided by the classical Lyapunov exponent.[21] In a similar manner, a quantitative measure of how much nearby particles separate after a specific amount of time has elapsed is provided by the FTLE.

In the early 1990s, Pierrehumbert[22] and Pierrehumbert and Yang[23] characterized atmospheric structures using FTLE fields. In particular, their work enabled the identification of both mixing regions and transport barriers. Later, in a series of papers published in the early 2000s, Haller[24–26] introduced the idea of LCS in order to provide a more rigorous, quantitative framework for the identification of fluid structures. Haller[26] proposed that the LCS be defined as a ridge of the FTLE field, and this idea was formalized several years later by Shadden, Lekien, and Marsden.[27] When computing the FTLE field of a dynamical system, these LCS, or ridges, are seen to be the structures which have a locally maximal FTLE value.

Although the FTLE/LCS theory can be extended to arbitrary dimension,[28] in this article we consider a 2D velocity field $\mathbf{v} : \mathbb{R}^2 \times I \to \mathbb{R}^2$ given by the deterministic part of Eqs. (1a)–(1c) which is defined over the time interval $I = [t_i, t_f] \subset \mathbb{R}$ and the following system of equations:

$$\dot{z}(t; t_i, z_0) = v(z(t; t_i, z_0), t), \qquad (2a)$$

$$z(t_i; t_i, z_0) = z_0, \qquad (2b)$$

where $\mathbf{z} = (x, y)^T \in \mathbb{R}^2$, $\mathbf{z}_0 \in \mathbb{R}^2$, and $t \in I$.

As previously stated, the trajectories of this dynamical system in the infinite time limits can be quantified with the system's Lyapunov exponents. If one restricts the Lyapunov exponent calculation to a finite-time interval, the resulting exponents are the FTLE. In practice, the FTLE computation involves consideration of nearby initial conditions and the determination of how the trajectories associated with these initial conditions evolve in time. Therefore, the FTLE provides a local measure of sensitivity to initial conditions and measures the growth rates of the linearized dynamics about the trajectories. Since the details of the derivation of the FTLE[24–29] as well as applications that employ the FTLE[30–32] have appeared in the literature, we shall only briefly summarize the procedure.

The solution of the dynamical system given by Eqs. (2a)–(2b) from the initial time $t_i$ to the final time $t_i + T$ can be viewed as the flow map $\phi_{t_i}^{t_i+T}$ which is defined as follows:

$$\phi_{t_i}^{t_i+T} : z_0 \mapsto \phi_{t_i}^{t_i+T}(z_0) = z(t_i + T; t_i, z_0). \qquad (3)$$

We consider an initial point located at $z$ at $t_i = 0$ along with a perturbed point located at $z + \delta z(0)$ at $t_i = 0$. Using a Taylor series expansion, one finds that

$$\delta z(T) = \frac{d\phi_{t_i}^{t_i+T}(z)}{dz} \delta z(0) + \mathcal{O}(\|\delta z(0)\|^2). \qquad (4)$$

Dropping the higher order terms, the magnitude of the linearized perturbations is given as

$$\|\delta z(T)\| = \sqrt{\langle \delta z(0), \Delta \rangle}, \qquad (5)$$

where $\Delta$ is the right Cauchy–Green deformation tensor and is given as follows:

$$\Delta(z, t_i, T) = \left( \frac{d\phi_{t_i}^{t_i+T}(z(t))}{dz(t)} \right)^* \left( \frac{d\phi_{t_i}^{t_i+T}(z(t))}{dz(t)} \right), \qquad (6)$$

with * denoting the adjoint. Then the FTLE can be defined as

$$\sigma(z, t_i, T) = \frac{1}{|T|} \ln \sqrt{\lambda_{\max}(\Delta)}, \qquad (7)$$

where $\lambda_{\max}(\Delta)$ is the maximum eigenvalue of $\Delta$.

For a given $z \in \mathbb{R}^2$ at an initial time $t_i$, Eq. (7) gives the maximum finite-time Lyapunov exponent for some finite integration time $T$ (forward or backward), and provides a measure of the sensitivity of a trajectory to small perturbations.

The FTLE field given by $\sigma(z, t_i, T)$ can be shown to exhibit ridges of local maxima in phase space. The ridges of the field indicate the location of attracting (backward time FTLE field) and repelling (forward time FTLE field) structures. In 2D space, the ridge is a curve which locally maximizes the FTLE field so that transverse to the ridge one finds the FTLE to be a local maximum.
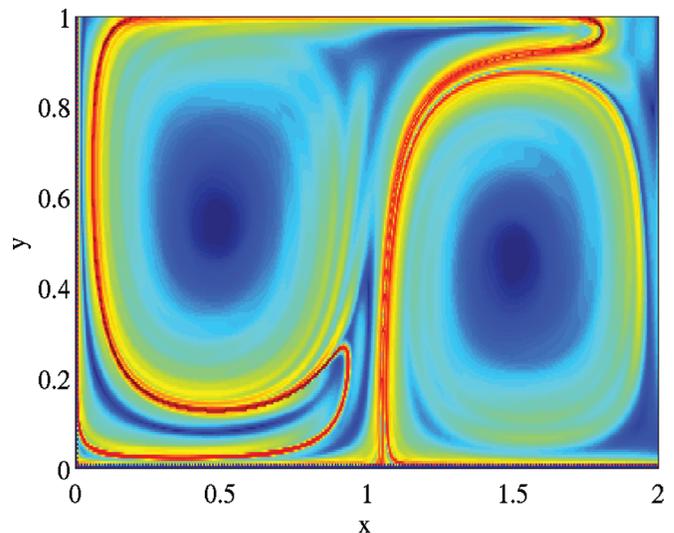


FIG. 3. (Color online) Forward FTLE flow field computed using the deterministic form of Eqs. (1a)–(1c) and shown at phase $\psi = 0$. The integration time is $T = 20$ with an integration step size of $t = 0.1$ and a grid resolution of 0.005 in both $x$ and $y$.

Figure 3 shows a snapshot taken at phase $\psi = 0$ of the forward time FTLE field calculated using the deterministic form of Eqs. (1a)–(1c) for a finite integration time $T = 20$. Figure 3 shows that there are ridges (in red) of locally maximal FTLE values. These ridges or LCS effectively separate the phase space into distinct dynamical regions. For the deterministic system, a particle placed in one of these distinct regions will remain in that region as the system evolves in time. Also, note that the red ridges appear to be a subset of the basin boundary set separating the two basins of attraction shown in Fig. 2.

In the stochastic system, the noise acts continuously on a particle placed in one of these distinct basins and, therefore, it is possible that the particle will cross the LCS and move into the other basin. Even though we find the LCS using the deterministic system, the location of these structures is a valuable tool in understanding how a particle escapes from the basin in which it is initially placed. Coupled with the ideas of uncertain sets and almost invariant sets described below, we will use the LCS information provided by the FTLE field to determine appropriate regions of control. In this way, it is possible to increase the loitering times of a particle in a basin while minimizing the amount of control actuation.

## IV. UNCERTAIN SETS

In this section, we describe a method that measures the fraction of uncertainty for regions in phase space. Nonlinear systems that possess multiple attractors typically can be extremely sensitive with respect to the choice of initial conditions. That is, very small changes, or uncertainty, in the initial conditions can lead to different attractors.[33–35] Sensitivity here is measured in the asymptotic time limit. When applied to high-dimensional attractors, long-time sensitivity is measured with respect to parameter sensitivity.[36] In contrast to the asymptotic definition, we measure uncertainty in
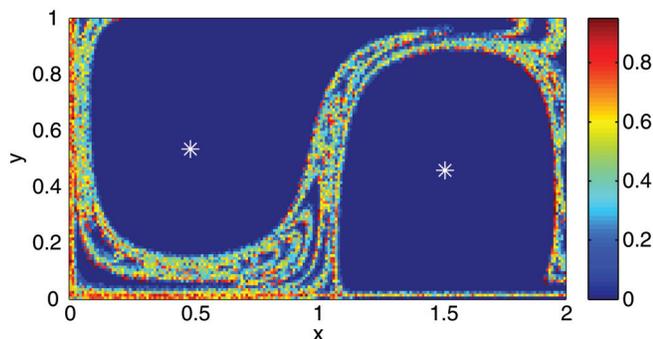
FIG. 4. (Color online) The uncertainty measure for the deterministic part of Eqs. (1a)–(1c) for the phase $\psi = 0$. A $200 \times 100$ regular grid of initial conditions is used. The color represents the fraction of trajectories that diverge from the trajectory of the center of each ball tested. The computation was performed using balls of radius $\epsilon = 0.02$ with 20 points chosen at random within each ball. The trajectories were computed until time $\tau = 400$ using a threshold parameter of 0.8.

phase space with respect to perturbations in initial data by computing exponential changes in distances over short time intervals.

The sensitivity of the deterministic system to the initial conditions is quantified by defining the pointwise uncertainty measure. For a point in phase space $(x_0, y_0)$ chosen at random, a ball of radius $\epsilon$ is constructed about that point, $B_\epsilon(x_0, y_0)$. For $N$ randomly chosen points in the ball $B_\epsilon(x_0, y_0)$, we record the number of trajectories, $N_\epsilon(\tau, x_0, y_0)$, at time $\tau$, that diverge beyond a certain distance from the trajectory of $(x_0, y_0)$. By diverge, we mean that we test if the distance between the trajectories at a given time is greater than a threshold parameter. The test indicates the fraction of initial conditions in the ball that diverge beyond a certain distance in a given finite time. If there are multiple attractors present, as $\tau \to \infty$, then the uncertain points correspond to those points that go to another basin. For finite $\tau$, as the radius of the ball is decreased, one obtains more accurate approximations of the basin boundary of the system. This is due to the fact that the dynamics are most sensitive with respect to the choice of initial conditions when the points straddle the basin boundary separating the basins of attraction.

Figure 4 shows a sample calculation of the uncertainty measure for the fixed phase $\psi = 0$. In this calculation, a $200 \times 100$ regular grid is used where each grid point coincides with the center of a ball of radius 0.02. By comparing the FTLE field shown in Fig. 3 with the uncertainty measure shown in Fig. 4, one can see that the location of the FTLE ridge is contained within the uncertainty region. In addition, it should be noted that the uncertainty measure captures the complicated fractal structure of the basin boundary shown in Fig. 2, as radius $\epsilon$ approaches zero. For the stochastic double-gyre, it is expected that the regions defined by the uncertain sets over all phases, $\psi \in [0, 20)$, will be the most active regions in which to actuate if one wishes to increase the residence time of a particle in one particular basin. We now refine this notion in the discrete case by defining the actual sets which will be almost invariant in the stochastic case. One may think of the almost invariant sets as the complement of the most uncertain regions in phase space.

## V. ALMOST INVARIANT SETS

As mentioned above, approximating the almost invariant sets is another method that can quantify where particles loiter in phase space for a stochastic system. Computation of the almost invariant sets will be achieved using the stochastic Frobenius–Perron operator. While the transition probabilities can be approximated for continuous time,[37] we take advantage of the fact that the double-gyre system is a periodically forced system. Therefore, the dynamics are sampled at a particular phase of the period. For small noise, contributions to the probability along trajectories come primarily from the difference between the tangent vector and the vector field. Averaging over a period of the drive allows one to sample the noise periodically. In doing this, we assume that the noise is not in the tail of the probability distribution so that there are no large, rare events. We, therefore, construct a Poincaré map with a specified noise distribution. This method of discrete sampling quantitatively identifies the complement of the uncertainty region as two almost invariant sets, which are associated with the stable attractors of the associated deterministic system. Although we present the machinery for a fixed phase, it is possible to extend the analysis for all phases of $\psi$, allowing one to approximate the density over the full forcing period.

To be explicit, consider a stochastically perturbed map $F_\eta : \mathbb{R}^n \to \mathbb{R}^n$, $x(t) \mapsto F(x(t)) + \eta$, where $\eta$ is a random variable having the distribution $v(x)$. Let $F(x(t))$ represent the map on the Poincaré section which samples the flow at time intervals of length $\tau$, equivalent to the period of the steady states. The SFP operator for a normal distribution with mean zero and standard deviation $\sigma$ is defined as[38]

$$P_F[\rho(x)] = \frac{1}{\sqrt{2\pi\sigma^2}} \int_M e^{-\frac{\|(x - F(y))\|^2}{2\sigma^2}} \rho(y) dy. \quad (8)$$

One approximates the density $\rho(x)$ by the finite sum of basis functions, $\rho(x) \simeq \sum_{i=1}^{N} c_i \phi_i(x)$, where $\phi_i(x) = \chi_{B_i}(x)$, and $\chi_B$ is an indicator defined on boxes $\{B_i\}_{i=1}^{N}$ covering the region $M$. The SFP operator is approximated by the $N \times N$ matrix,

$$A_{ij} \equiv A(B_i, B_j) = (P_F[\phi_j], \phi_i) = \int_M P_F[\phi_j(x)]\phi_i(x)dx \quad (9)$$

for $1 \leq i, j \leq N$. Therefore, a transition matrix entry $A_{ij}$ value represents how mass, or measure, flows from cell $B_i$ to cell $B_j$. Details of the method can be found in Ref. 39.

From the transition matrix, a reversible Markov chain is constructed, satisfying $\pi_i A_{ij} = \pi_j A_{ji}$ for all $i, j$. Such a condition implies $\pi$ is an invariant (stationary) distribution of $A$.[40] Since, in general, $A$ is not reversible as it is defined in Eq. (9), a reversible Markov chain is constructed from the transition matrix. Let $R = (A + \hat{A})/2$, where $\hat{A}_{ij} = (\pi_j/\pi_i)A_{ji}$ and $\pi$ is an invariant probability density of $A$. The matrix $R$ now possesses detailed balance.

Since $R$ is reversible, it has the properties that its eigenvalues are real and the eigenvectors are orthogonal. One can then compute a collection of sets which are almost invariant by examining the eigenvectors of $R$. A gauge of how much

(a)

(b)
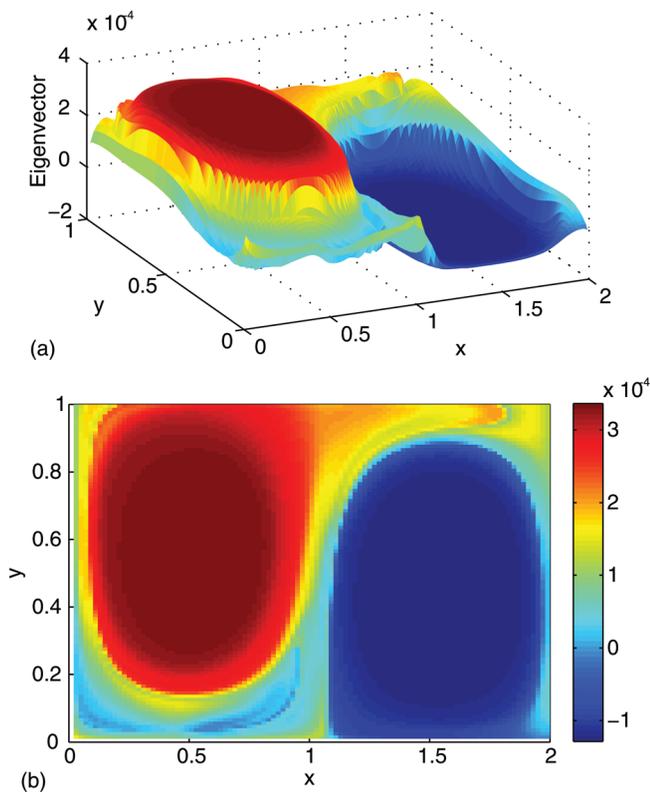
FIG. 5. (Color online) The results of approximating the almost invariant sets for the stochastic system given by Eqs. (1a)–(1c) at the phase $\psi = 0$. A $100 \times 100$ grid of points is used with a standard deviation of $\sigma = 0.05$. Figure 5(a) is the mapping of the second eigenvector of the reversible matrix back to the phase space. The almost invariant sets are represented by the red and the blue regions at the ends of the eigenvector range. Figure 5(b) is the contour plot of the surface, which shows the transition region that forms a barrier between the almost invariant sets.

measure is ejected each iterate from the defined almost invariant sets is given by the eigenvalues. The first few eigenvalues of $R$ will be clustered near unity and their associated eigenstates will be a mixture of almost invariant sets formed from the above basis elements. Since the first eigenvector of $R$ is a vector of ones, the second eigenvector is used to identify two almost invariant sets emanating from basins of attraction. The fact that the eigenvalues cluster near unity means that very little mass is ejected from the basins each iterate, which is due to the basins are defined as almost invariant states.

The results of the almost invariant sets computation are shown in Fig. 5 for the Poincaré map of the double-gyre at $\psi = 0$. The second eigenvector can be visualized by a roughly piecewise constant function, with a transition region connecting the two pieces. The eigenvalue associated with this eigenvector is 0.9996. The higher level represents the left basin (red) and the lower level represents the right basin (blue). For this computation, a $100 \times 100$ grid of points is used with a standard deviation of $\sigma = 0.05$. As expected, the complement set of the left and right almost invariant basins agrees approximately with the location of the uncertain region from Fig. 4.

## VI. CORRAL CONTROL IN THE PRESENCE OF FLUCTUATIONS

Since we have now computed the location of the LCS and have approximated the most uncertain regions and almost
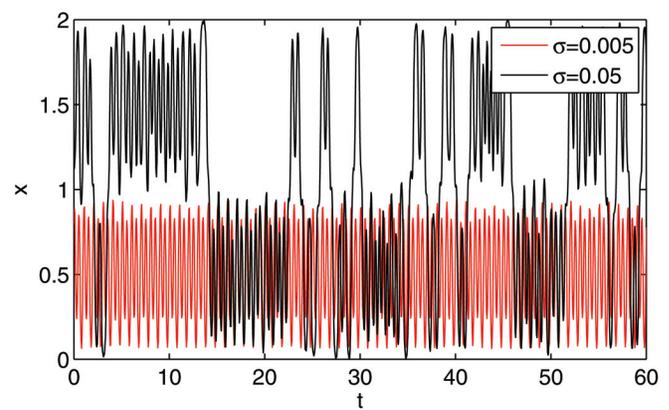


FIG. 6. (Color online) A graph of the $x -$ coordinate for two simulations of the stochastic system given by Eqs. (1a)–(1c). For continuous noise with standard deviation $\sigma = 0.005$, one does not observe switching events (red). However, for the larger standard deviation of $\sigma = 0.05$, one can see frequent switching between the two basins (black).

invariant regions of phase space, we can consider loitering, or residence times, within a defined region. Moreover, we may use actuation to control trajectories in the system by increasing the loitering times within an almost invariant set. To quantify the residence time of a particle in a basin, we consider the double-gyre system with continuously added Gaussian noise. As the standard deviation, $\sigma$, of the noise is increased, trajectories wander in larger neighborhoods about the stable steady states and frequently switch from one basin to another, as shown in Fig. 6. These basins are approximated by the almost invariant sets at a fixed phase, shown in Fig. 5.

The control strategy employs a monitoring ball (that we refer to as a control region) that covers the almost invariant set with the center defined as the left nonboundary steady state when time $t = 0$. When a trajectory passes beyond a threshold distance from the center $(x_s, y_s)$ of the control region, a radial force is turned on. This force moves the trajectory back toward the center of the region. This control strategy can be modeled as

$$\dot{x} = -\pi A \sin(\pi f(x, t)) \cos(\pi y) - \alpha x + \eta_1(t) \\ - c(x - x_s)\Theta(r(x, y) - r_0), \tag{10a}$$

$$\dot{y} = \pi A \cos(\pi f(x, t)) \sin(\pi y)\frac{df}{dx} - \alpha y + \eta_2(t) \\ - c(y - y_s)\Theta(r(x, y) - r_0), \tag{10b}$$

$$f(x, t) = \epsilon \sin(\omega t + \psi)x^2 + (1 - 2\epsilon \sin(\omega t + \psi))x, \tag{10c}$$

$$r(x, y) = \sqrt{(x - x_s)^2 + (y - y_s)^2}, \tag{10d}$$

where $c$ is the magnitude of the control force, $r_0$ is the radial threshold, and $\Theta$ is a Heaviside function. By adjusting $r_0$ and $c$, it is possible to control the number of actuations and the effectiveness of the control scheme. We have designed this specific control strategy to take advantage of the underlying flow structure in order to corral the particles into the almost invariant set. We therefore refer to our scheme as corral control.

The control scheme is tested by observing the changes in the almost invariant sets. Figure 7 shows the results of approximating the almost invariant sets for the stochastic
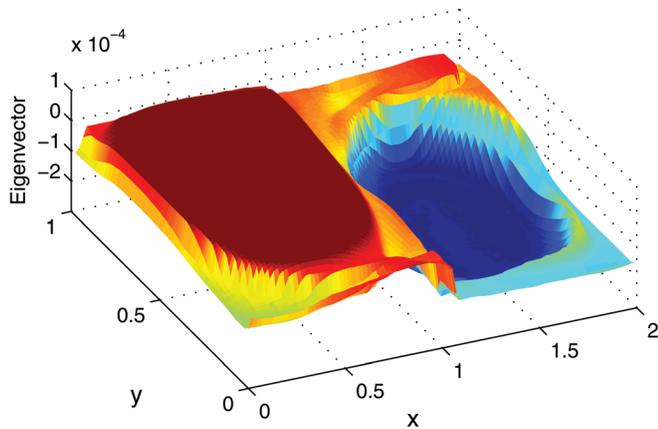
FIG. 7. (Color online) The results of approximating the almost invariant sets for the stochastic system with control applied to the left basin given by Eqs. (10a)–(10d) at the phase $\psi = 0$. A $100 \times 100$ grid of points with a standard deviation of $\sigma = 0.05$ is used. Similar to Fig. 5(a), this graph is the mapping of the second eigenvector of the reversible matrix back to the phase space. The almost invariant sets are represented by the red and the blue regions at the ends of the eigenvector range. One can see that the Fig. 7 left basin (red) is larger than the Fig. 5(a) left basin, while the Fig. 7 right basin (blue) is smaller than the Fig. 5(a) right basin.

system with control applied to the left basin given by Eqs. (10a)–(10d) for $c = 0.25$. As expected, there is an increase in the size of the left (red) almost invariant set and a decrease in the size of the right (blue) almost invariant set when compared to Fig. 5.

We have analyzed how individual trajectories escape under this control algorithm. By measuring the most frequent path of an escape event from the left basin to the right basin, one can observe that the trajectories follow the FTLE ridge toward a periodic saddle orbit on the $x$ axis. Topologically, the FTLE ridge loops around the almost invariant sets, corralling points in the outlying region to the other side. The goal is to reduce the number of escape events by a control algorithm that takes advantage of the topology of the system.

Figures 8(a)–(c) illustrate the topology (as does a movie which can be found as auxiliary online material URL: http://dx.doi.org/10.1063/1.3539836.1). In these figures, 20,000 particles were placed in the left basin near the fixed point and their trajectories were tracked. If a particle crossed the $x = 1.2$ threshold, the particle was considered to have escaped from the left basin into the right basin. In Figs. 8(a)–(c), the color contours show the probability density of the trajectory path prehistory for all the particles (there are 4361 of them) that escaped from the left basin between phases $\psi \in [0.65, 0.7]$. The prehistory shows that there are many paths to escape. However, the high-probability density in the region of the saddle [near the point $(1, 0)$] shows that most of the particles have been funneled into the saddle region just prior to escape from the left basin. Also shown in the figures are the position of the particles (black dots) before escape, the FTLE contour, and a circular region of radius $r = 0.4$ that denotes the control region. These last three features are shown at phase $\psi = 0.0$ in Fig. 8(a), at phase $\psi = 0.25$ in Fig. 8(b), and at phase $\psi = 0.5$ in Fig. 8(c). The control force used in this simulation is $c = 0.15$.

Figure 8(a) shows that, although many particles are outside the control region, the majority of the particles are
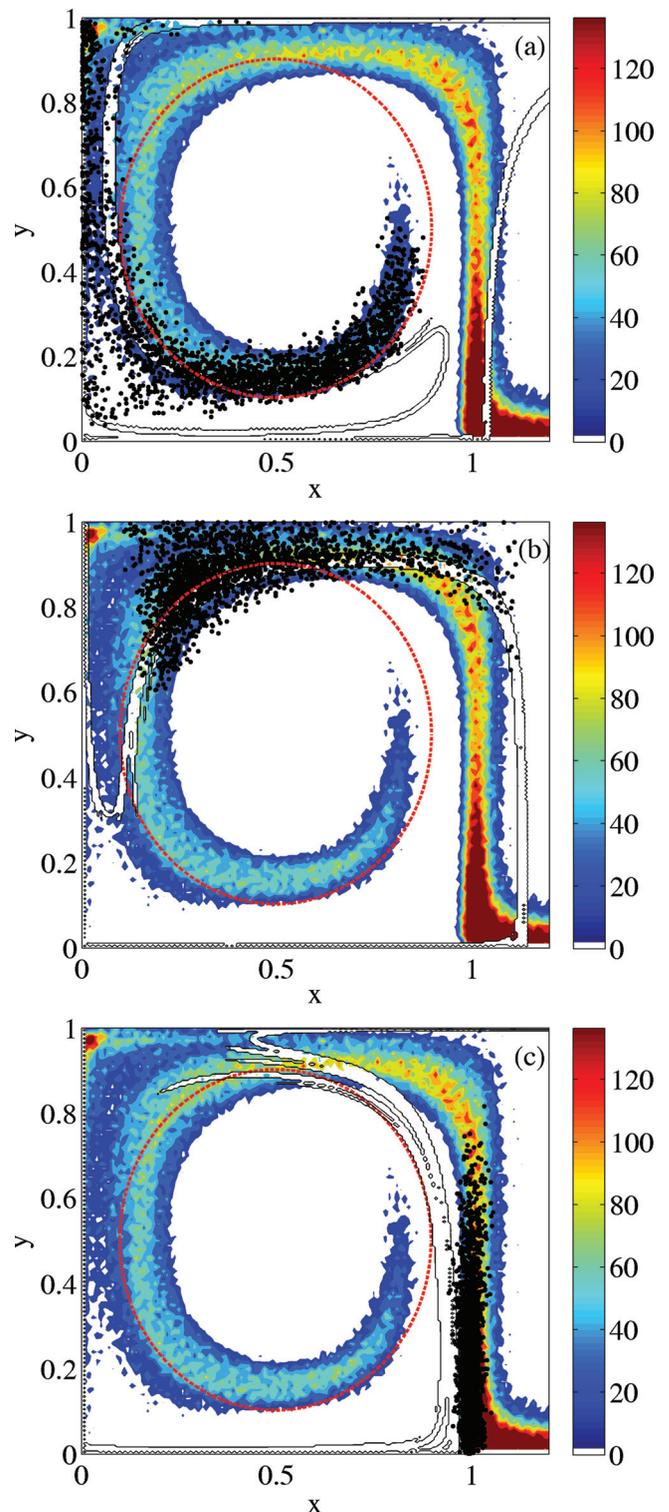


FIG. 8. (Color online) Probability density of the trajectory path prehistory for particles that escaped from the left basin based on a threshold of $x = 1.2$ between phases $\psi \in [0.65, 0.7]$. These paths form a subset of 20000 random particle simulations. Also shown is the position of the particles (black dots) before escape, the FTLE ridge (black curve), and the control region of radius $r = 0.4$ (red) at (a) phase $\psi = 0.0$, (b) phase $\psi = 0.25$, and (c) phase $\psi = 0.5$. The control force is $c = 0.15$ (enhanced online). [URL: http://dx.doi.org/10.1063/1.3539836.1]

inside the control region. For those particles that are inside the control region, no control is being applied. In addition, the majority of the particles lie on one side of the FTLE ridge, which is bounding the almost invariant set (from

comparison with Fig. 5). As time evolves, one can see in Fig. 8(b) that the FTLE ridge sweeps up the left side of the figure, and one can see from the prehistory that about half of the particles sweep up the left side, staying on the exterior side of the FTLE ridge outside the control region so that the control is actuated. The other half of the particles remain on the interior side of the FTLE ridge inside the control region so that no control is actuated.

Eventually, as can be seen in Fig. 8(c), the FTLE ridge enters the region of uncertainty (see Fig. 5), and all the particles cross over the FTLE ridge. All the particles now have left the control region. However, even though the control is being actuated, it cannot overcome the underlying dynamics found in this system and all the particles will proceed toward the saddle and finally escape. To prevent escape and to increase loitering time, one can use the knowledge of the location of the FTLE ridge, uncertainty regions and almost invariant sets to design a control region. For example, by choosing a control region with a smaller radius, one can prevent the particles from approaching the FTLE ridges and uncertain areas. With such a small radius, however, the number of control actuations will be very large. Control actuation may be optimized by using a control region with the largest possible radius so that the region does not intersect the FTLE structures.

## A. Scaling of the mean escape time with respect to noise and control

We vary the control parameter, $c$, to study its effect on the mean escape time. One expects that an increase in $c$ will lead to a corresponding increase in the mean time to escape. Note that since the control force is finite, there is always a finite probability of escape even if control is actuated. The control algorithm decreases the probability of trajectories visiting the regions that have a high probability of transition, and the mean time to escape reflects the decrease in PDF in the transition regions.

Figure 9(a) shows the natural log of the average escape time as a function of the inverse of the noise intensity. One can see that as the control force is increased, the mean time to escape increases with the slope depending linearly on the control parameter. Since small changes in $c$ translate into exponential changes in residence times, one recovers a linear relation of the slope of the exponent as a function of $c$ which can be seen in Fig. 9(b).

## B. Optimizing control actuations

Another consideration is that one would like to minimize the number of actuations for the particle, thereby preserving the energy needed to employ the control scheme. As a consequence, this could extend the use of a battery in an autonomous underwater glider. Figure 10 shows the natural log of the average number of actuations per unit time as a function of the control radius. For $r \leq 0.36$, the FTLE ridge does not intersect the control region and the average number of actuations follows the scaling of the average escape time. Beyond that, the number of actuations increases as the control scheme works to move the trajectory back inside the control region. Therefore, the number of actuations per unit
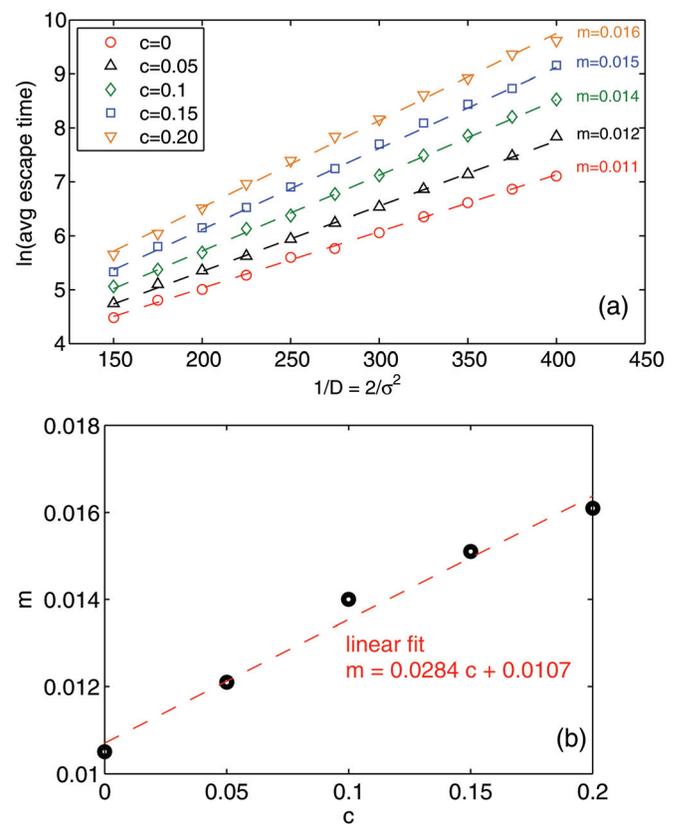


FIG. 9. (Color online) (a) Natural log of the average escape time as a function of the inverse of the noise intensity. The control radius is $r = 0.4$ and a threshold of $x = 1.2$ is used to identify escape from the left basin. The results are averaged over 1000 simulations and the slopes of the linear fit to each data set are noted on the right. (b) The slopes of the average escape time linear fits from Fig. 9(a) as a function of the control parameter $c$.

time follows the average escape rate for $r \leq 0.36$ and the minimum number of actuations can be found for the largest control region inside the FTLE ridge.

## C. One-dimensional analysis of control

To understand the effectiveness of the control scheme and its scaling properties, we approximate the natural probability
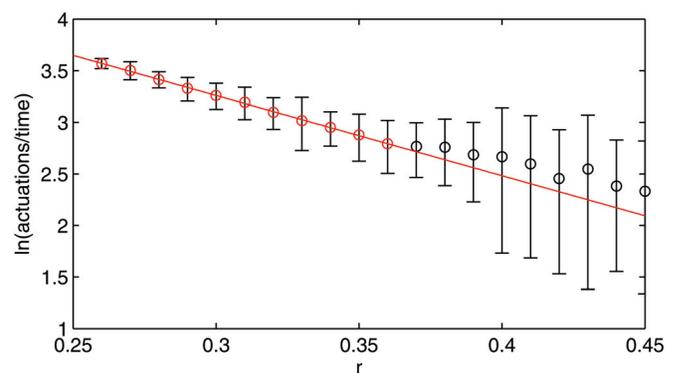


FIG. 10. (Color online) Natural log of the average number of actuations per unit time as a function of the control radius for parameters $\sigma = 0.075$ and $c = 0.25$. The mean number of actuations ($\circ$) was calculated over 100 simulations of time series with $t \leq 10^5$, or until an escape event occurred. The error bars show one standard deviation of the data from the mean. Overlaid is a linear fit for the data points $r \leq 0.36$, since for this range of $r$ the control region does not intersect the FTLE ridge.
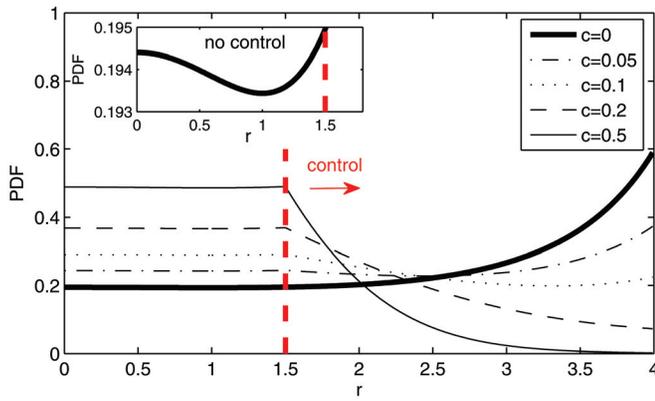
FIG. 11. (Color online) PDF as a function of the control radius $r$ for varying control force $c$ found using Eq. (13). Continuous noise is used with $\sigma = 1$, $\lambda = 0.1$, and $\epsilon = 1.5$. The normalization constant, $\kappa$, was set in each case so that the area under the curve is one. The inset shows a close-up of the PDF near the attractor for the case of no control.

density function (PDF) and the almost invariant set in the following 1D example. Consider a stochastic system, where the deterministic part has a stable focus at the origin surrounded by an unstable limit cycle. In the associated deterministic system, the points inside the limit cycle would spiral toward the stable focus, while the points outside would diverge. The stochastic perturbations allow trajectories to escape across the limit cycle (and then diverge), creating an almost invariant set. This captures the local behavior in one basin of the double-gyre. Now consider a control region with radius $\epsilon > 0$, where $\epsilon$ determines the distance from the attractor for which the control is actuated. Then the system has the form

$$\frac{d}{dt}\begin{bmatrix} x \\ y \end{bmatrix} = \begin{bmatrix} -\lambda & \omega \\ -\omega & -\lambda \end{bmatrix}\begin{bmatrix} x \\ y \end{bmatrix} + \lambda\begin{bmatrix} x \\ y \end{bmatrix}(x^2 + y^2)$$
$$- c\Theta(r - \epsilon)\begin{bmatrix} x \\ y \end{bmatrix} + \boldsymbol{\eta}(t), \tag{11}$$

where $\lambda, \omega > 0$. As before, $c$ is the magnitude of the control force and $\Theta$ is a Heaviside function. Each component of $\boldsymbol{\eta}(t) = [\eta_1(t), \eta_2(t)]^T$ is a random variable with intensity $D$.

To find the PDF, we switch to polar coordinates using the time-dependent change of variables given by $x = r\cos\theta$ and $y = r\sin\theta$. This results in the following transformed stochastic system:

$$\dot{r} = \lambda r(r^2 - 1) - cr\Theta(r - \epsilon) + \eta_1(t)\cos\omega t - \eta_2(t)\sin\omega t. \tag{12}$$

Here, we find that $\theta = -\omega t$ and the noise vanishes entirely from the $\theta$ equation.

Assuming the transformed noise term still has intensity $D$ and $\kappa$ is a normalization constant, the probability density $\rho(r)$, is given by

$$\rho(r) = \kappa\exp\left(\frac{\lambda}{4D}(r^2(r^2 - 2)) - \frac{c}{2}(r^2 - \epsilon^2)\Theta(r - \epsilon)\right). \tag{13}$$

The PDF is now fully specified by the deterministic flow and noise drift, control strength, and actuation region, and can be plotted for various parameters.
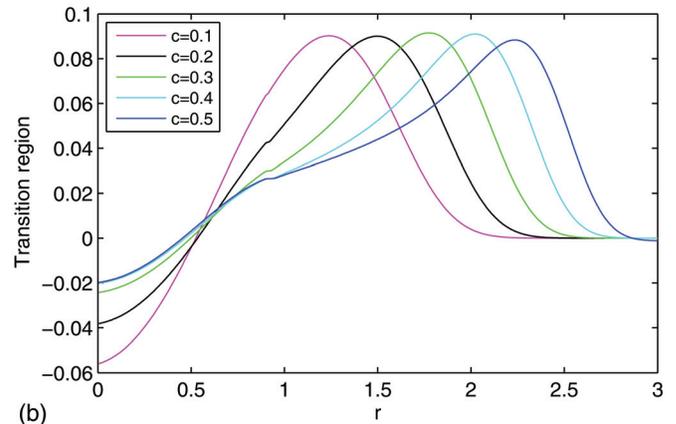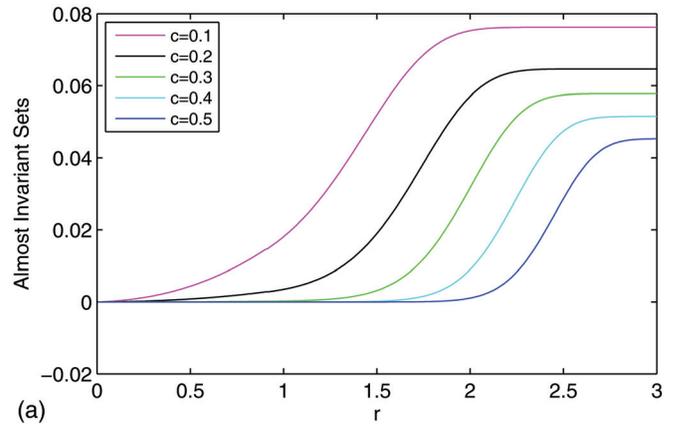


FIG. 12. (Color online) The results of the almost invariant set analysis for varying control force $c$ in Eq. (12) with $\lambda = 0.1$, $\epsilon = 0.9$, and Gaussian noise with standard deviation of $\sigma = 0.1$. Figure 12(a) shows the almost invariant set for varying control force $c$. The second eigenvector of the transport matrix is mapped back to the domain $r$. Note that as $c$ increases, the right basin extends to the right. Figure 12(b) shows the transition set for varying control force $c$. The third eigenvector of the transport matrix is mapped back to the domain $r$. Note that as $c$ increases, the transition region moves to the right.

Figure 11 shows that an increase in the control strength decreases the probability of the trajectory moving outside the boundary of the control region. The inset figure shows that the local minimum of the PDF occurs at $r = 1$, which is the location of the unstable limit cycle. The PDFs branch at the point of control at $r = 1.5$. The thick solid curve represents the dynamics with no control. It follows that a trajectory escaping outside the limit cycle will diverge to infinity, and the PDF increases as the value of $r$ increases.

In addition, one can perform the one-dimensional almost invariant set analysis for this example. The transport matrix is computed using a grid of 500 intervals on the domain and Gaussian noise with standard deviation of $\sigma = 0.1$. The point of control is located at $r = 0.9$, to the left of the basin boundary at $r = 1$. Figure 12(a), shows the expansion of the left almost invariant set to the right as the control is increased. This information is contained in the second eigenvector of the transport matrix. The lower and upper almost constant regions of the function represent location of the sets. Figure 12(b) shows the movement of the transport region to the right as the control is increased. This information is contained in the third eigenvector of the transport matrix. The maximum

value of the function represents the location of the transition region. Notice that it is the complement of the almost invariant sets.

Both the PDF and almost invariant set analysis demonstrate the change that the control algorithm has on the natural dynamics of the stochastic system. The control algorithm decreases the probability of trajectories visiting regions where deterministic dynamics would cause them to diverge. This moves the effective basin boundary farther from the attractor, increasing its size. By using sufficient control radius and force, any trajectory that would naturally diverge can be redirected toward the attractor. Therefore, the almost invariant set can be expanded to the desired size at a cost of the number of control actuations.

Additionally, it is possible to quantify the relation between the mean escape time and the potential defined by the PDF. Using the well-known Kramer's escape rate,[41] one can predict the rate at which a particle can escape over a potential barrier under Brownian motion. In one dimension, the escape time of a particle from a potential defined by $U(x)$ is $\tau = (2\pi/\sqrt{U''(x_a)|U''(x_f)|}) \exp[(U(x_f) - U(x_a))/D]$, where $x_a$ is the location of the attractor and $x_f$ is the location of the escape point. From the radial control PDF given by Eq. (13), one can see that the potential function exponent depends linearly on the control amplitude $c$. All of these one-dimensional analytic results are consistent with the behavior seen for the double-gyre system with control that was presented in the preceding subsections.

## VII. CONCLUSIONS

Using modern dynamical systems theory, we have analyzed the flow of a stochastic double-gyre as a model of a wind-driven ocean. The existence of multiple almost invariant sets combined with highly uncertain regions in phase space gives rise to stochastic switching between the basins. The uncertain regions generate high-probability transition sets which are the primary cause of switching from one basin to another. We showed that the high probability of transitions may be approximated by computing uncertain regions with respect to initial conditions and the use of FTLE.

The system displays maximum sensitivity near the deterministic basin boundary trajectory. Knowledge of the FTLE ridges in a given flow, in conjunction with knowledge of uncertain regions and almost invariant sets, enables one to predict the location of escape trajectories from one basin to another. As in previous work,[42] these transition regions may be monitored directly to predict future switching events. This knowledge, in turn, allows for set-based corral control methods to be used to inhibit the escape event and increase the loitering time within the basin.

Almost invariant sets were computed explicitly using the Frobenius–Perron theory for discrete stochastic systems. The sets provided approximate target regions in which to control particles which act as sensors in large surveillance regions. That is, given initial conditions in one of the almost invariant basins, the particles will stay in the sets for long, but finite time. Although computed for a discrete map model, the sets approximate well the continuous noise almost invari-

ant sets. They also form sets of the most certain points in that they are the complement of the uncertain region, which was computed based on initial condition uncertainty.

Since the almost invariant sets are indicative of long-time, but finite, dynamics, we used these sets or subsets to define corral control regions in which we wish to maintain the residence times in one basin with minimal control actuation. To this end, we designed a simple discrete controller to extend the residence times in the continuous noise double-gyre. We find that even small control amplitudes have an exponential increase on the residence times. This is quite similar to the well-known problem of noise-induced escape from a potential well, even though the basin boundaries may be fractal in the deterministic case.

We saw that if the control radius defined a set which did not intersect the ridges defined by the FTLE, the number of actuations per unit time followed an exponential law as a function of noise intensity. This can be understood completely from the switching rate theory. On the other hand, if the control radius intersected the FTLE ridge, the uncertainty regions were breached, and the control actuation rate no longer follows a nice scaling law, but rather some complicated function of control radius $r$.

The model presented here is a simplified version of a double-gyre flow that is a solution to a realistic quasi-geostrophic ocean model, and the vehicles controlled are point particles. However, the techniques here can be extended to full ocean and glider models in the future. The extensions to vehicles with real mass means that inertial effects will need to be included in 3D GFD models. However, the machinery presented here is well-suited to the description of sets in higher dimensions, and we expect that the monitoring of large surveillance regions in the ocean by gliders will be enhanced by implementing our corral control method. Additionally, the study and control of coupled systems, with and without delay, is of interest.

### APPENDIX: DETAILS OF THE OCEAN MODEL

The ocean model results in Fig. 1 were obtained by numerical solution of barotropic quasi-geostrophic flow in a single-layer basin $\Omega := [0, 1] \times [0, 1]$ on a $\beta$ plane. The governing nondimensionalized equation for the fluid streamfunction $\Psi$ is

$$\frac{\partial \nabla^2 \Psi}{\partial t} + \epsilon J(\Psi, \nabla^2 \Psi) + \frac{\partial \Psi}{\partial x} = \mu \nabla^2 \Psi + W, \qquad (A1)$$

where $J$ is the Jacobian operator,

$$J(f,g) := \frac{\partial f}{\partial x}\frac{\partial g}{\partial y} - \frac{\partial g}{\partial x}\frac{\partial f}{\partial y}, \qquad (A2)$$

and forcing is provided by a wind-stress curl, $W$, that is prescribed as follows to form a double-gyre circulation with a weak periodic "seasonal" variation:

$$W = -\sin 2\pi y + 2\alpha\pi \sin \omega t, \qquad (A3)$$

where the amplitude $\alpha = 0.1$ and frequency $\omega = 3$ were used to produce Fig. 1.

This system is characterized by the nondimensional parameters[43]

$$\mu = \frac{R}{\beta L} \text{ and } \epsilon = \frac{U}{\beta L^2}, \qquad (A4)$$

where $\beta$ is the rotation parameter, $R$ is the bottom friction and $L$ and $U$ are, respectively, the characteristic length and velocity scales of the basin. The parameters $\mu$ and $\epsilon$ correspond to the relative length scales of the Stommel and inertial layers, respectively. To produce Fig. 1, we used $\mu = 0.04$ and $\epsilon = 0.0004$.

The above model has been numerically integrated using second-order spatial differences and second-order Runge-Kutta time stepping for the streamfunction, and a fourth-order Runge-Kutta algorithm to compute the Lagrangian trajectories of tracer particles. In Fig. 1, a grid of resolution $64^2$ was used and a dimensionless time step of $dt = 0.001$. Coordinates of tracer particles are independent of the grid while flow velocities at the particle locations are found using bilinear interpolation from the grid values. An initially static ocean spins-up in a few hundred time steps. If $\alpha = 0$ the spun-up solution is stationary, while nonzero $\alpha$ leads to a superimposed oscillatory behavior. The tracers are held in place until spin-up is complete.

[1]J. Harlim, M. Oczkowski, J. A. Yorke, E. Kalnay, and B. R. Hunt, Phys. Rev. Lett. **94**, 228501(2005).

[2]D. C. Webb, P. J. Simonetti, and C. P. Jones, IEEE J. Ocean. Eng. **26**, 447 (2001).

[3]J. Sherman, R. E. Davis, W. B. Owens, and J. Valdes, IEEE J. Ocean. Eng. **26**, 437 (2001).

[4]C. C. Eriksen, T. J. Osse, R. D. Light, T. Wen, T. W. Lehman, P. L. Sabin, J. W. Ballard, and A. M. Chiodi, IEEE J. Ocean. Eng. **26**, 424 (2001).

[5]M. Weldon, T. Peacock, G. Jacobs, M. Helu, and G. Haller, J. Fluid Mech. **611**, 1 (2008).

[6]E. Villermaux, P. Marmottant, and J. Duplat, Phys. Rev. Lett. **92**, 074501 (2004).

[7]T. Boeck, J. Li, E. López-Pagés, P. Yecko, and S. Zaleski, Theor. Comput. Fluid Dyn. **21**, 59 (2007).

[8]H. Aref, J. Fluid Mech. **143**, 1 (1984).

[9]T. Dombre, U. Frisch, J. Greene, M. Hénon, A. Mehr, and A. Soward, J. Fluid Mech. **167**, 353 (1986).

[10]A. Provenzale, Annu. Rev. Fluid Mech. **31**, 55 (1999).

[11]S. Wiggins, Annu. Rev. Fluid Mech. **37**, 295 (2005).

[12]K. Ide, D. Small, and S. Wiggins, Nonlinear Processes Geophys. **9**, 237 (2002).

[13]P. S. Berloff and S. P. Meacham, J. Mar. Res. **55**, 407 (1997).

[14]B. T. Nadiga and B. P. Luce, J. Phys. Oceanogr. **31**, 2669 (2001).

[15]R. Meucci, D. Cinotti, E. Allaria, L. Billings, I. Triandaf, D. Morgan, and I. B. Schwartz, Physica D **189**, 70 (2004).

[16]E. Forgoston and I. B. Schwartz, SIAM J. Appl. Dyn. Syst. **8**, 1190 (2009).

[17]E. Forgoston, L. Billings, and I. B. Schwartz, Chaos **19**, 043110 (2009).

[18]H. Yang and Z. Liu, Geophys. Res. Lett. **21**, 545 (1994).

[19]V. Rom-Kedar, A. Leonard, and S. Wiggins, J. Fluid Mech. **214**, 347 (1990).

[20]G. Froyland and K. Padberg, Physica D **238**, 1507 (2009).

[21]J. Guckenheimer and P. Holmes, *Nonlinear Oscillations, Dynamical Systems, and Bifurcations of Vector Fields* (Springer-Verlag, New York, 1986).

[22]R. T. Pierrehumbert, Phys. Fluids A **3**, 1250 (1991).

[23]R. T. Pierrehumbert and H. Yang, J. Atmos. Sci. **50**, 2462 (1993).

[24]G. Haller, Chaos **10**, 99 (2000).

[25]G. Haller, Physica D **149**, 248 (2001).

[26]G. Haller, Phys. Fluids **14**, 1851 (2002).

[27]S. C. Shadden, F. Lekien, and J. E. Marsden, Physica D **212**, 271 (2005).

[28]F. Lekien, S. C. Shadden, and J. E. Marsden, J. Math. Phys. **48**, 065404 (2007).

[29]M. Branicki and S. Wiggins, Nonlinear Processes Geophys. **17**, 1 (2010).

[30]W. Tang, P. W. Chan, and G. Haller, Chaos **20**, 017502 (2010).

[31]J. D. Eldredge and K. Chong, Chaos **20**, 017509 (2010).

[32]S. Lukens, X. Yang, and L. Fauci, Chaos **20**, 017511 (2010).

[33]C. Grebogi, S. W. McDonald, E. Ott, and J. A. Yorke, Phys. Lett. A **99**, 415 (1983).

[34]S. W. McDonald, C. Grebogi, E. Ott, and J. A. Yorke, Physica D **17**, 125 (1985).

[35]Y.-C. Lai, C. Grebogi, and E. J. Kostelich, Phys. Lett. A **196**, 206 (1994).

[36]I. B. Schwartz, Y. K. Wood, and I. T. Georgiou, Comput. Phys. Commun. **121–122**, 425 (1999).

[37]H. Risken, *The Fokker–Planck Equation* (Springer-Verlag, Berlin, 1996).

[38]L. Billings, E. M. Bollt, and I. B. Schwartz, Phys. Rev. Lett. **88**, 234101 (2002).

[39]E. M. Bollt, L. Billings, and I. B. Schwartz, Physica D **173**, 153 (2002).

[40]J. L. Doob, *Stochastic Processes* (Wiley, New York, 1990).

[41]H. A. Kramers, Physica **7**, 284 (1940).

[42]I. B. Schwartz, L. Billings, and E. M. Bollt, Phys. Rev. E **70**, 046220 (2004).

[43]J. Pedlosky, *Ocean Circulation Theory* (Springer, New York, 1996).